NANO LETTERS

Letter

pubs.acs.org/NanoLett

# Signatures of Phonon and Defect-Assisted Tunneling in Planar Metal–Hexagonal Boron Nitride–Graphene Junctions

U. Chandni,*[,†] K. Watanabe,[‡] T. Taniguchi,[‡] and J. P. Eisenstein[†]

[†]Institute for Quantum Information and Matter, Department of Physics, California Institute of Technology, 1200 East California Boulevard, Pasadena, California 91125, United States

[‡]National Institute for Materials Science, 1-1 Namiki Tsukuba, Ibaraki 305-0044, Japan

Supporting Information

**ABSTRACT:** Electron tunneling spectroscopy measurements on van der Waals heterostructures consisting of metal and graphene (or graphite) electrodes separated by atomically thin hexagonal boron nitride tunnel barriers are reported. The tunneling conductance, $dI/dV$, at low voltages is relatively weak, with a strong enhancement reproducibly observed to occur at around $|V| \approx 50$ mV. While the weak tunneling at low energies is attributed to the absence of substantial overlap, in momentum space, of the metal and graphene Fermi surfaces, the enhancement at higher energies signals the onset of inelastic processes in which phonons in the heterostructure provide the momentum necessary to link the Fermi surfaces. Pronounced peaks in the second derivative of the tunnel current, $d^2I/dV^2$, are observed at voltages where known phonon modes in the tunnel junction have a high density of states. In addition, features in the tunneling conductance attributed to single electron charging of nanometer-scale defects in the boron nitride are also observed in these devices. The small electronic density of states of graphene allows the charging spectra of these defect states to be electrostatically tuned, leading to "Coulomb diamonds" in the tunneling conductance.

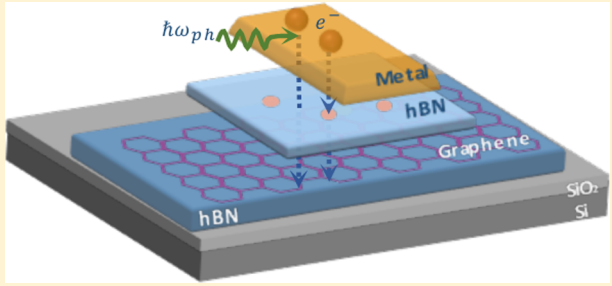


**KEYWORDS:** *Tunneling, graphene, hexagonal boron nitride, hBN, hBN defects, Coulomb blockade, phonon-assisted tunneling, IETS*

Tunneling spectroscopy has proven to be an excellent tool for studying low-dimensional electronic systems.[1,2] In addition to revealing features pertaining to the density of states (DOS) of the junction electrodes,[3] tunneling can probe the geometry of the electrode Fermi surfaces,[4,5] electron–electron interactions both within and between the electrodes,[6] phonon energy scales,[7] defects within the tunnel barrier,[8] etc. While scanning tunneling microscopy (STM) is extensively used as a sensitive tool to detect the local DOS,[9] macroscopic planar tunnel junctions provide averaged properties over larger length scales, often demanding reliable and reproducible device fabrication methods. In the former, tunneling occurs at the atomic tip of the STM probe, thus involving electrons with a wide range of transverse momenta. In contrast, smooth planar tunnel junctions offer the possibility of momentum-resolved tunneling spectroscopy.[3−5,10]

Recent advances in creating van der Waals heterostructures based on graphene and hexagonal boron nitride (hBN) have opened new avenues to creating atomically smooth tunnel junctions.[11,12] hBN is an isomorph of graphene with ∼2% lattice mismatch and has been the preferred substrate material for high-mobility graphene devices.[13] Its large insulating band gap of ∼5.9 eV and atomically smooth layers make hBN a good tunnel barrier candidate, which can potentially aid in-plane momentum conservation. Previous studies on simple metal–insulator–metal junctions with hBN as the insulator showed a linear current–voltage ($IV$) characteristic around zero-bias.[8,14,15] The observed exponential dependence of the conductance on the hBN thickness established hBN as a good crystalline tunnel barrier. However, it was also observed that intrinsic nanometer-scale defect states present in the hBN atomic layers act like quantum dots and contribute to the tunneling $IV$ characteristics via single-electron charging events.[8] In related works on graphene-hBN-graphene junctions, features seen in the $IV$ characteristic were attributed to resonant processes conserving the in-plane momentum and chirality of the tunneling electrons.[16−18]

In this work, we investigate tunnel junctions in which 2–5 atomic layers of hBN (thickness of $\lesssim$2 nm) are sandwiched between a graphene (or graphite) electrode and a conventional metal counter-electrode. Several distinct features of our results stand out. Most dramatically, in all devices studied, the tunneling conductance $dI/dV$ exhibits an abrupt and pronounced enhancement at bias voltages in excess of roughly ±50 mV. Our measurements reveal this enhancement to arise from a series of sharp peaks in the second derivative of the tunnel current, $d^2I/dV^2$. The voltage locations of these peaks coincide with specific phonon modes in the heterostructure and

**Received:** October 18, 2016
**Revised:** November 17, 2016
**Published:** November 28, 2016

ACS Publications © 2016 American Chemical Society



DOI: 10.1021/acs.nanolett.6b04369
*Nano Lett.* 2016, 16, 7982–7987

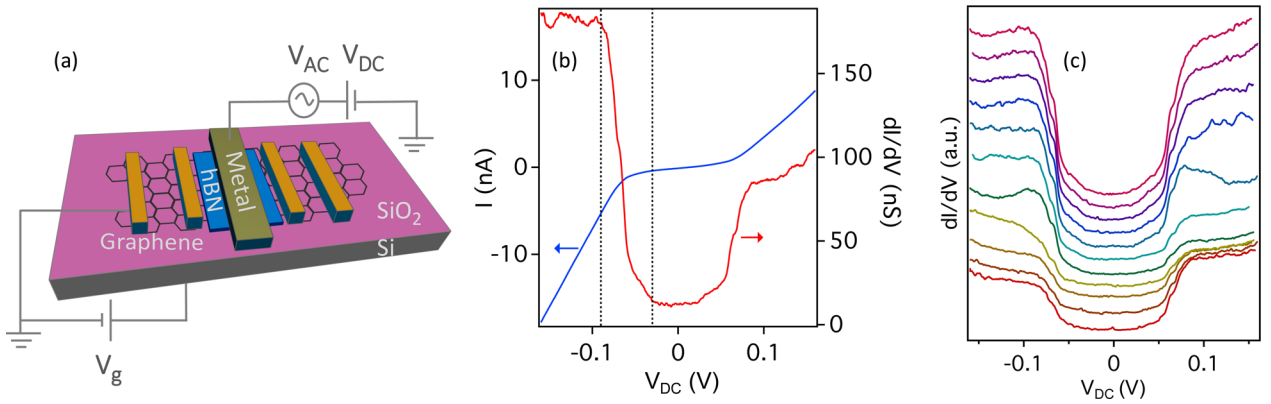


**Figure 1.** (a) General schematic of our device structure, with $SiO_2$−Si acting as the substrate and a thin hBN as the tunnel barrier (not to scale). Gate voltage is applied to the $SiO_2$(~285 nm) dielectric layer. An AC + DC bias is applied to the top metal tunnel electrode (Ag or Cr−Au), and the tunnel current is measured using one of the Ohmic contacts (Cr−Au) to the bottom graphene layer. (b) Tunnel current ($I$) and differential conductance d$I$/d$V$ as a function of source-drain bias ($V_{DC}$) for a monolayer graphene device at zero gate voltage. The dotted vertical lines are at $V_{DC}$ = −30 and −90 mV. (c) d$I$/d$V$ at every 10 V from $V_g$ = +50 (bottom) to −50 V (top). The curves are offset for clarity.

are insensitive to a voltage applied to a back gate underlying the tunnel junction. At lower bias, below the onset of phonon-assisted tunneling, we find that the tunneling conductance does respond to a back-gate voltage, with a minimum in the conductance observed when the graphene is close to the Dirac point. Finally, sharp features arising from Coulomb charging of intrinsic defect states in the hBN barrier layer are also sometimes observed. Due to incomplete screening by the graphene electrode, these defect signatures also respond to a back gate voltage, and the classic "diamond pattern" associated with Coulomb blockade is seen.

The present tunnel junctions consist of a mono- or bilayer graphene (MLG or BLG) or graphite lower electrode, a thin (≤5 atomic layers) hBN tunnel barrier, and a metallic (either Cr−Au or Ag) top electrode. These junctions are assembled on a $SiO_2$ substrate or on a thick hBN layer mounted on $SiO_2$. In all cases, the 285 nm thick $SiO_2$ layer itself lies atop a p-doped Si wafer that serves as a back gate and provides mechanical support.

To create these van der Waals heterostructures, graphene (or graphite) and hBN flakes are first mechanically exfoliated onto separate Si wafers (also overlaid with $SiO_2$). For tunnel devices with $SiO_2$ as the substrate material, the mechanically exfoliated graphene/graphite layer acts as the bottom electrode. For tunnel devices with hBN as the substrate material, the graphene/graphite layer is first transferred onto a thick hBN layer atop a $SiO_2$ substrate using the polymer-stamp dry-transfer technique described in ref 13. Next, the thin hBN tunnel barrier is similarly transferred on to the graphene/graphite. Finally, the metallic top tunnel electrode is lithographically fabricated by depositing Cr−Au (5/120 nm) or Ag (120 nm). Lateral dimensions of the junctions vary from ~2 × 2 to 6 × 6 $\mu m^2$.

The electrical transport properties of the graphene layer are measured using additional Cr−Au electrodes. A schematic of a typical device is shown in Figure 1a. Tunneling current−voltage ($IV$) and differential conductance d$I$/d$V$ characterictics are measured simultaneously using standard lock-in techniques ($V = V_{DC} + V_{AC}$, with $V_{AC}$ = 0.5 mV at 13 Hz). The $d^2I/dV^2$ measurements were also performed simultaneously using a second lock-in amplifier synchronized at twice the excitation frequency. All of the measurements were done at $T$ = 4.2 K.

Figure 1(b) displays $IV$ and d$I$/d$V$ characteristics from a tunnel junction consisting of a monolayer graphene lower electrode, a hBN tunnel barrier, and a Cr−Au top electrode, all assembled on $SiO_2$−Si. As the figure makes clear, a small but finite tunneling conductance is observed at $V_{DC}$ = 0. Around $|V_{DC}| \approx 30$ mV, d$I$/d$V$ begins to rise rapidly before leveling off beyond about $|V_{DC}| \approx 90$ mV.

Applying a back-gate voltage ($V_g$) to the doped Si substrate tunes the free carrier density and, given the Dirac-like spectrum of MLG, the electronic density of states in the MLG electrode. Figure 1c shows that the strong finite voltage enhancement of d$I$/d$V$ is unaffected by the back gate voltage, at least for $-50 \leq V_g \leq +50$ V. In contrast, the magnitude of the tunneling conductance around $V_{DC}$ = 0 does depend on the back gate voltage. This is illustrated in Figure 2a, where the blue dots give the average tunneling conductance ⟨d$I$/d$V$⟩ over the range $|V_{DC}| \leq 20$ mV, while the red trace shows the measured resistivity $\rho_{MLG}$ of the graphene sheet. Although not precisely coincident, the minimum in ⟨d$I$/d$V$⟩ occurs at nearly the same gate voltage as the maximum in the graphene resistivity. Hence, consistent with expectations, the tunneling conductance is minimized at the Dirac point, where the graphene density of states is lowest and its resistivity highest. Figure 2b shows the tunneling conductance d$I$/d$V$ as a function of both $V_g$ and $V_{DC}$ on a logarithmic color scale. The finite voltage enhancement of d$I$/d$V$ appears as a vertical blue-colored band of uniform width, while the dark blue spot near $V_g$ = 20 V locates the graphene Dirac point.

To elucidate the origin of these features in the tunneling characteristics, additional devices were fabricated with variations in the tunnel electrodes and the underlying substrate material. Figure 3a−c shows tunnel characteristics for three such devices consisting of (a) a MLG-hBN-Cr−Au tunnel junction, assembled on hBN substrate; (b) a BLG-hBN-Ag tunnel junction, assembled on $SiO_2$−Si substrate; and (c) a graphite-hBN-Cr−Au tunnel junction assembled on $SiO_2$−Si substrate, respectively. As is evident, the abrupt strong enhancement of the tunneling conductance at finite voltage is observed in all the devices measured independent of the substrate, the type of graphene/graphite electrode, and the metal forming the top tunnel electrode. Similar signatures were observed in 14 tunnel junctions from 8 devices.



DOI: 10.1021/acs.nanolett.6b04369
Nano Lett. 2016, 16, 7982−7987

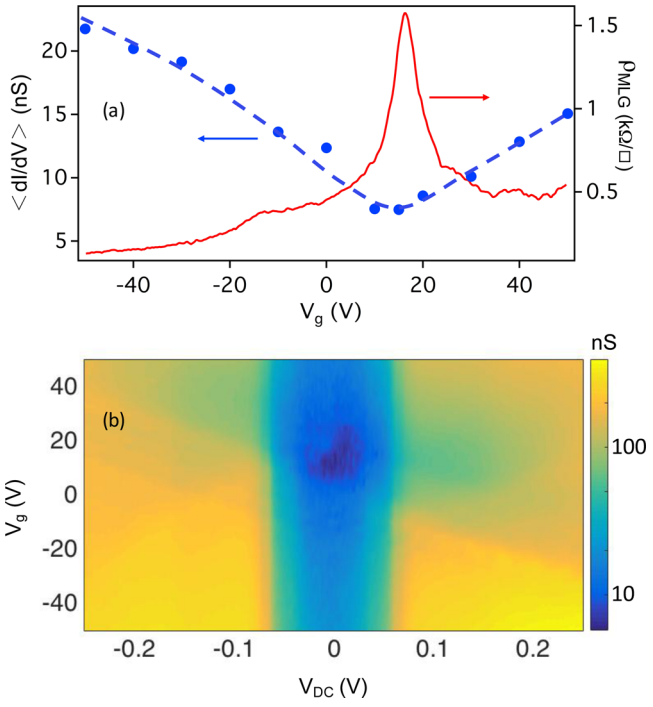


**Figure 2.** (a) Average conductance around zero-bias $\langle dI/dV \rangle$ (blue) as a function of back-gate voltage ($V_g$) for the MLG device in Figure 1b,c. The dashed line is a guide to the eye. The corresponding graphene resistivity ($\rho_{MLG}$) vs back-gate voltage is plotted in red. (b) A colormap of the differential conductance, $dI/dV$, plotted in a log scale as a function of the back-gate voltage and source-drain bias.

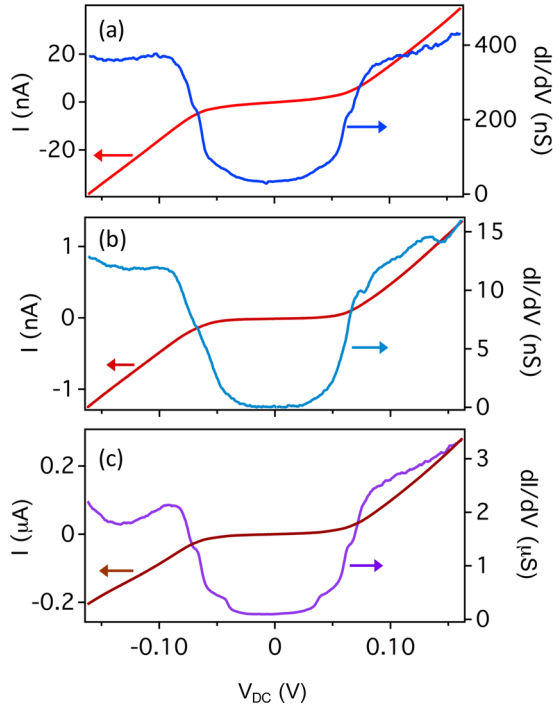


**Figure 3.** Tunnel current ($I$) and differential conductance ($dI/dV$) as a function of source-drain bias ($V_{DC}$) for (a) a MLG-hBN-Cr−Au tunnel junction on hBN substrate, (b) BLG-hBN-Ag tunnel junction on $SiO_2$−Si substrate, and (c) graphite-hBN-Cr−Au on $SiO_2$−Si substrate.

We begin the discussion of these tunneling results with an idealized and oversimplified model. If in-plane momentum is perfectly conserved, then the tunneling conductance at zero bias will vanish unless the Fermi surfaces (FS) of the two electrodes overlap in momentum space. In graphene, the FS consists of tiny circles located at the $K$ and $K'$ points of the hexagonal Brillouin zone. These points lie $1.70 \times 10^{10}$ m$^{-1}$ away from the zone center. In contrast, for an idealized free electron metal the FS is a sphere at the zone center. For silver, the radius of this sphere is $k_{F,Ag} \approx 1.2 \times 10^{10}$ m$^{-1}$. Hence, in this approximation, there is no overlap between the graphene and silver Fermi surfaces, and thus, the zero bias tunneling conductance vanishes (at low temperature).

As Figure 3 clearly shows, our tunnel junctions do in fact exhibit a nonzero, if small, tunneling conductance at zero bias. The fact that, in our MLG-hBN-Cr−Au junctions, the average low-bias conductance depends on the linear density of states of the graphene electrode demonstrates that this conductance is dominated by tunneling, not some parasitic conducting channel between the electrodes. Although we do not know for certain from where this low-bias tunneling conductance originates, there are a variety of possibilities. For example, the Fermi surfaces of the metal and graphene/graphite electrodes may in fact overlap. While this seems unlikely in the case in which the metal electrode is Ag, the Cr−Au case is less clear. For those junctions, the 5 nm Cr layer underlying the Au is most relevant. The FS of Cr is highly complex and very far from a free electron sphere.[19] Although the large electron pocket at the Cr zone center does not overlap with the $K$ and $K'$ points of graphene, the hole pockets around the vertices of the Cr Brillouin zone can. The degree of this overlap is hard to assess, given the polycrystalline nature of the Cr layer (see the Supporting Information for a discussion on the Fermi surfaces of Cr, Ag, and graphene). For perfect in-plane momentum conservation, the atomic smoothness of the barrier layer and the quality of the interfaces are crucial factors. While the former criterion is satisfied by the exfoliated layers of hBN, the interfaces, particularly those between the hBN barriers and the evaporated polycrystalline metal electrodes, can be uneven and disordered. This could be a potential reason for the finite zero-bias conductivity via imperfect tunneling channels.

At finite bias, tunneling via various inelastic processes can occur.[20−23] In particular, phonons can provide the momentum needed to overcome the FS mismatch and allow tunneling to proceed. As the data in Figure 3 suggests, the rapid enhancement of the tunnel conductance at finite bias occurs in a series of steps, better resolved in some junctions than in others. To examine these features more closely, the second derivative of the tunnel current, $d^2I/dV^2$, was recorded. Figure 4 shows typical results, with Figure 4a showing the $d^2I/dV^2$ spectrum from a graphite-hBN-Cr−Au tunnel junction and Figure 4b the spectrum from a MLG-hBN-Cr−Au device. As is apparent, the spectra are virtually identical and show no gate-voltage dependence (Figure 4c). A total of four prominent peaks, labeled A, B, C, and D in the figure, are seen in each polarity. Averaged over six devices, the voltage location of these peaks are $|V_A| = 36 \pm 3$ mV, $|V_B| = 61 \pm 2$ mV, $|V_C| = 74 \pm 2$ mV, and $|V_D| = 166 \pm 8$ mV. As discussed below, we associate these peaks with phonon-assisted inelastic tunneling processes.

The phonon spectra of graphene, graphite, and hBN are all quite similar due to their closely matched crystal structures.[24−26] The energies of the various acoustic and optical phonons in these materials are all in the range below about 200 meV and are thus obvious candidates for explaining the various peaks in $d^2I/dV^2$. Moreover, because the electronic momentum



DOI: 10.1021/acs.nanolett.6b04369
Nano Lett. 2016, 16, 7982−7987

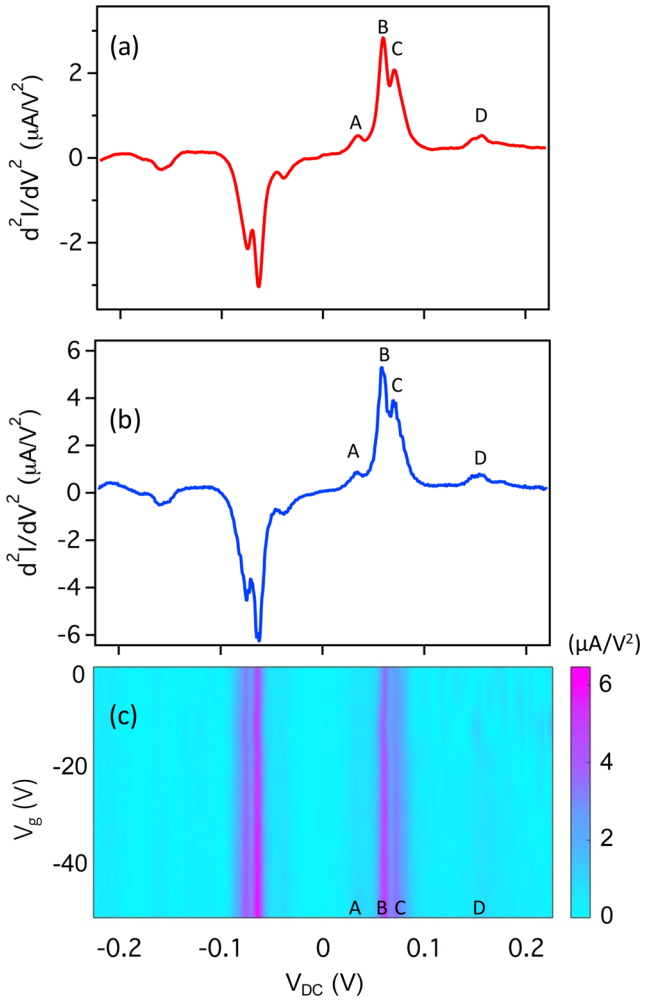


**Figure 4.** (a) Derivative of conductance ($d^2I/dV^2$) as a function of source-drain bias ($V_{DC}$) for a graphite-hBN-Cr−Au tunnel junction. A total of four phonon peaks are marked as A−D. (b) $d^2I/dV^2$ vs $V_{DC}$ for a MLG-hBN-Cr−Au tunnel junction, averaged over the gate voltage range 0 to −50 V. (c) The absolute value of the $d^2I/dV^2$ as a function of $V_g$ and $V_{DC}$ for the MLG device in (b). The phonon peaks A−D are found to be gate voltage independent.

component perpendicular to the tunneling plane is not conserved, there is considerable phase space for in-plane phonons to link the three-dimensional FS of the metal with the two-dimensional FS of the graphene. Tunneling thus proceeds with electrons in the metal using their $z$-momenta and a phonon mode from either the hBN or the graphene layer to tunnel on to the graphene layer (see Figure S2). A quantitative analysis of the kinematics of phonon-assisted tunneling requires a detailed knowledge of the electrode Fermi surfaces. While the FS of graphene (and graphite) are well-approximated as tiny circles at the corners of their Brillouin zones, the FS of the metal electrodes is not so simple. This is particularly true for Cr whose Fermi surface is very complex.[19] For this reason, we confine our analysis to a search for those energies at which the phonon density of states is particularly large.

The phonon dispersion in hBN shows a flat band, and thus a high phonon density of states, along a line connecting the $M$ and $K$ points in the Brillouin zone at ∼40 meV;[25] this is close to peak A shown in the $d^2I/dV^2$ spectra shown in Figure 4. Similarly, multiple flat bands and crossings are present in the phonon dispersions of both hBN and graphene in the energy range of ∼60−75 meV,[24,25] where we observe the two strongest peaks, B and C, in $d^2I/dV^2$. Around 150−170 meV, where peak D resides, both materials again possess a large phonon density of states. A more detailed discussion of phonon-assisted tunneling in our devices can be found in the Supporting Information. We note that while tunneling dominates our transport, unintentional point contacts in the tunnel junction may have a minor contribution to the observed conductance and phonon modes.

Interestingly, previous works on tunneling in van der Waals heterostructures employing graphene/graphite-hBN-graphene junctions have reported a series of phonon modes.[22,23] While in these reports, the tunneling occurs between the FS of the graphene (and graphite) layers in the plane, with a possible rotational misalignment between the two layers, in the current experiment, a three-dimensional spherical metal surface is involved. Here, the polycrystallinity of the metal electrode and the hBN−metal interface disorder can lead to weaker coupling to the phonon modes as compared to the much-cleaner graphene− and graphite−hBN interfaces. Consequently, we observe fewer peaks compared to those studies. We also note that when stacked as a heterostructure with restricted phase space and compressive strains, the phonon modes in the graphene and hBN layers may have slightly different energies as compared to their free-standing counterparts or to those reported in other heterostructure configurations.[22,23] We also observe that the peak D in our case is much broader than peaks A−C. Possibly, the out-of-plane phonon modes contribute significantly to our tunneling spectra, with sharp peaks at corresponding energies (A−C), which agrees with previous reports that the out-of-plane phonons couple signficantly to the graphene $\pi$−electrons.[20]

In addition to the features discussed above, weak tunneling features are seen in some junctions. Figure 5a shows the $dI/dV$ characteristic for a BLG-hBN-Ag tunnel junction on Si−$SiO_2$ substrate, for various gate voltages. While the strong, finite voltage enhancement is a robust feature of the tunneling conductance, weak additional peaks, marked by arrows in the figure, are observed to shift around with gate voltage. Figure 5b presents a color map of the conductance as a function of $V_g$ and $V_{DC}$ showing, that these features evolve as sharp lines crossing in a roughly diamond pattern. Similar signatures were also observed in a MLG-hBN-Ag tunnel junction on Si−$SiO_2$ substrate, as seen in Figure 5c. The average tunneling conductance for this junction was much larger than for the device used for Figure 5b, most likely owing to a thinner hBN barrier, but the numerous weak features in the vicinity of $V_{DC}$ = 0 again exhibit a clear diamond pattern. Interestingly, while the gate voltage dependent features are seen as peaks in $dI/dV$ in Figure 5a,b, they appear as dips in Figure 5c.

Although the hBN layers used in van der Waals heterostructures are often assumed to be pristine defect-free single crystals, this is not always the case. Our previous experiments on metal−hBN−metal (M−hBN−M) junctions revealed that is some cases, the $IV$ curve exhibits a staircase-like pattern very reminiscent of the Coulomb staircase observed in tunneling through a quantum dot.[8] Similar signatures were also obtained in graphite−hBN−graphite junctions fabricated using a dry-transfer pick-up method, which resulted in lower amount of residues, indicating that the fetaures are intrinsic to the heterostructure. This suggests that tunneling in M−hBN−M junctions can proceed via a two-step process involving tunneling from one metal electrode to a defect in the hBN


DOI: 10.1021/acs.nanolett.6b04369
Nano Lett. 2016, 16, 7982−7987

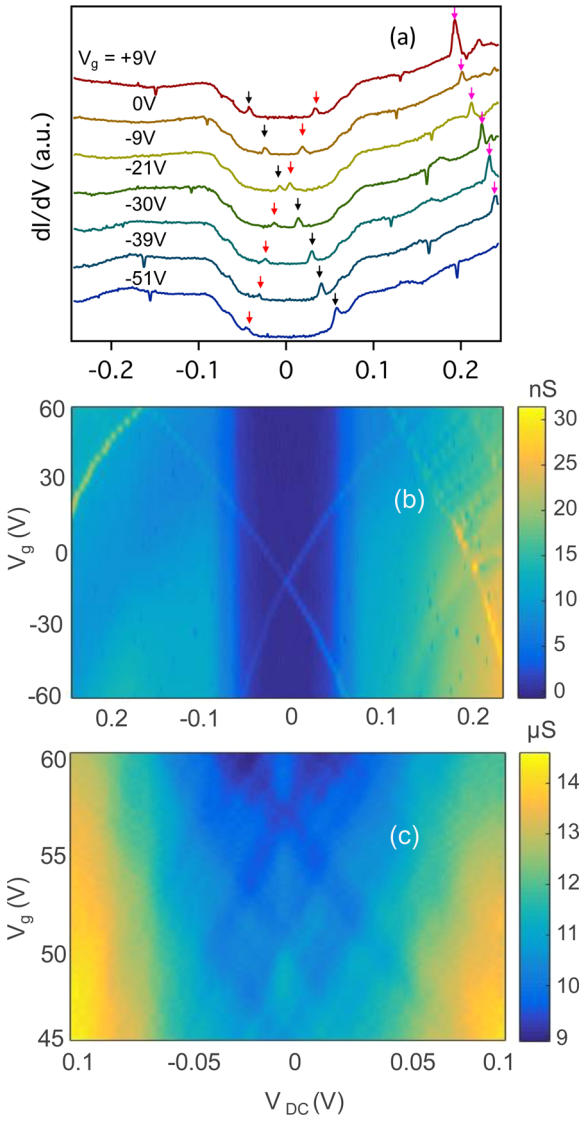


**Figure 5.** (a) Conductance plots at various gate voltages for a BLG-hBN-Ag tunnel junction. The curves are offset for clarity. The arrows elucidate additional gate voltage dependent features. Color map of conductance plotted as a function of gate voltage and source-drain bias for (b) the BLG device in (a) and (c) a MLG-hBN-Ag tunnel junction. The average mobilities of the two devices were $\mu \approx 4800$ cm$^2$/(V s) and 5500 cm$^2$/(V s), respectively, typical of graphene devices on Si–$SiO_2$ substrates.

and then from the defect to the other metal electrode. From the voltage scale of the steps in the *IV* curve, the size of the defect was estimated to be in the few nanometer range, similar to that found in STM experiments that directly imaged defects in thin hBN layers.[27] In such M–hBN–M devices, the metal electrodes very effectively screen out external gate electric fields. As a result, the classic diamond pattern was not observed.

In graphene–hBN–metal tunnel junctions, the graphene lower electrode has such a low density of states that it cannot entirely screen an electric field produced by the underlying doped Si gate. This imperfect screening, often referred to as a "quantum capacitance" effect, has been widely observed in both graphene[28] and semiconductor heterostructures.[29] In the present experiments, that portion of the gate electric field, which penetrates through the graphene layer electrostatically shifts the energy of charged defects in the hBN layer and allows the diamond pattern to be observed.

We speculate that the dips in Figure 5c might reflect Fano resonances.[30,31] Interference of a resonant state with a continuum (nonresonant background) leads to Fano line shapes in various nanostructures. When the coupling to the leads is strong and the nonresonant contribution to the conductance is of the same order as the resonant component, the line shapes of the conductance as a function of $V_g$ become unusual. When the nonresonant contribution dominates, symmetric dips are obtained in conductance versus $V_g$, in place of standard Coulomb oscillation peaks. In Figure 5c, the background nonresonant component dominates, as is evident from the large conductance ($\sim\mu$S). In Figure5a,b, the nonresonant component is much lower ($\sim$ nS), and we obtain Coulomb peaks and the usual diamond pattern.

In summary, tunneling spectroscopy measurements on metal–hBN–graphene (or graphite) junctions reveal clear signatures of both phonon-assisted and defect-assisted tunneling processes. Phonon-assisted tunneling is particularly prominent in these devices owing to the small, and in some cases vanishing, overlap between the Fermi surfaces of the metal and the graphene (or graphite) electrodes. This lack of overlap sharply limits the phase space for direct, momentum conserving, electron tunneling. A total of four prominent peaks in the second derivative of tunneling current, $d^2I/dV^2$, are associated with known phonons in the van der Waals heterostructure. In addition, disorder, including point-like defects, in the hBN barrier layer enable tunneling events, which do not conserve in-plane momentum. In some devices, weak peaks in the tunneling conductance were found to present a diamond pattern when examined as a function of back gate voltage. This confirms our prior conclusion that these peaks reflect single-electron charging of nm-scale defects in the hBN layer.

## ■ ASSOCIATED CONTENT

### Supporting Information

The Supporting Information is available free of charge on the ACS Publications website at DOI: 10.1021/acs.nanolett.6b04369.

Description of phonon-assisted tunneling and the role played by the Fermi surfaces. (PDF)

## ■ AUTHOR INFORMATION


### Corresponding Author

*E-mail: chandniu@gmail.com.

### ORCID

U. Chandni: 0000-0002-4275-2687


### Notes

The authors declare no competing financial interest.

## ■ ACKNOWLEDGMENTS

We thank S. Das Sarma, T. Klapwijk, R. Sensarma and L. Zhao for useful discussions, and G. Rossman for the use of his Raman spectroscopy facility. Atomic force microscopy was done at the Molecular Materials Research Center of the Beckman Institute at the California Institute of Technology. This work was supported by the Institute for Quantum Information and Matter, an NSF Physics Frontiers Center with support of the



DOI: 10.1021/acs.nanolett.6b04369
*Nano Lett.* 2016, 16, 7982–7987

Gordon and Betty Moore Foundation through Grant No. GBMF1250.

## REFERENCES

(1) Smoliner, J. *Semicond. Sci. Technol.* **1996**, *11*, 1−16.
(2) Wolf, E. L. *Principles of Electron Tunneling Spectroscopy*, (Oxford University Press, Oxford, 1985).
(3) Reed, M. A.; Randall, J. N.; Aggarwal, R. J.; Matyi, R. J.; Moore, T. M.; Wetsel, A. E. *Phys. Rev. Lett.* **1988**, *60*, 535−537.
(4) Eisenstein, J. P.; Gramila, T. J.; Pfeiffer, L. N.; West, K. W. *Phys. Rev. B: Condens. Matter Mater. Phys.* **1991**, *44*, 6511−6514.
(5) Gennser, U.; Kesan, V. P.; Syphers, D. A.; Smith, T. P.; Iyer, S. S.; Yang, E. S. *Phys. Rev. Lett.* **1991**, *67*, 3828−3831.
(6) See, for example, Eisenstein, J. P.; Pfeiffer, L. N.; West, K. W. *Phys. Rev. Lett.* **1992**, *69*, 3804−3807.
(7) Chynoweth, A. G.; Logan, R. A.; Thomas, D. E. *Phys. Rev.* **1962**, *125*, 877−881.
(8) Chandni, U.; Watanabe, K.; Taniguchi, T.; Eisenstein, J. P. *Nano Lett.* **2015**, *15*, 7329−7333.
(9) Chen, C. J. *Introduction to Scanning Tunneling Microscopy*, (Oxford University Press, Oxford, 2008).
(10) Smoliner, J.; Demmerle, W.; Berthold, G.; Gornik, E.; Weimann, G. *Phys. Rev. Lett.* **1989**, *63*, 2116−2119.
(11) Britnell, L.; Gorbachev, R. V.; Jalil, R.; Belle, B. D.; Schedin, F.; Mishchenko, A.; Georgiou, T.; Katsnelson, M. I.; Eaves, L.; Morozov, S. V.; Peres, N. M. R.; Leist, J.; Geim, A. K.; Novoselov, K. S.; Ponomarenko, L. A. *Science* **2012**, *335*, 947−950.
(12) Amet, F.; Williams, J. R.; Garcia, A. G. F.; Yankowitz, M.; Watanabe, K.; Taniguchi, T.; Goldhaber-Gordon, D. *Phys. Rev. B* **2012**, *85*, 073405.
(13) Wang, L.; Meric, I.; Huang, P. Y.; Gao, Q.; Gao, Y.; Tran, H.; Taniguchi, T.; Watanabe, K.; Campos, L. M.; Muller, D. A.; Guo, J.; Kim, P.; Hone, J.; Shepard, K. L.; Dean, C. R. *Science* **2013**, *342*, 614−617.
(14) Lee, G.-H.; Yu, Y.-J.; Lee, C.; Dean, C.; Shepard, K. L.; Kim, P.; Hone, J. *Appl. Phys. Lett.* **2011**, *99*, 243114.
(15) Britnell, L.; Gorbachev, R. V.; Jalil, R.; Belle, B. D.; Schedin, F.; Katsnelson, M. I.; Eaves, L.; Mozorov, S. V.; Mayorov, A. S.; Peres, N. M. R.; Castro Neto, A. H.; Leist, J.; Geim, A. K.; Ponomarenko, L. A.; Novoselov, K. S. *Nano Lett.* **2012**, *12*, 1707−1710.
(16) Mishchenko, A.; Tu, J. S.; Cao, Y.; Gorbachev, R. V.; Wallbank, J. R.; Greenaway, M. T.; Morozov, V. E.; Morozov, S. V.; Zhu, M. J.; Wong, S. L.; Withers, F.; Woods, C. R.; Kim, Y.-J.; Watanabe, K.; Taniguchi, T.; Vdovin, E. E.; Makarovsky, O.; Fromhold, T. M.; Falko, V. I.; Geim, A. K.; Eaves, L.; Novoselov, K. S. *Nat. Nanotechnol.* **2014**, *9*, 808−813.
(17) Wallbank, J. R.; Ghazaryan, D.; Misra, A.; Cao, Y.; Tu, J. S.; Piot, B. A.; Potemski, M.; Pezzini, S.; Wiedmann, S.; Zeitler, U.; Lane, T. L. M.; Morozov, S. V.; Greenaway, M. T.; Eaves, L.; Geim, A. K.; Fal'ko, V. I.; Novoselov, K. S.; Mishchenko, A. *Science* **2016**, *353*, 575−579.
(18) Fallahazad, B.; Lee, K.; Kang, S.; Xue, J.; Larentis, S.; Corbet, C.; Kim, K.; Movva, H. C. P.; Taniguchi, T.; Watanabe, K.; Register, L. F.; Banerjee, S. K.; Tutuc, E. *Nano Lett.* **2015**, *15*, 428−433.
(19) Fawcett, E. *Rev. Mod. Phys.* **1988**, *60*, 209−283.
(20) Zhang, Y.; Brar, V. W.; Wang, F.; Girit, C.; Yayon, Y.; Panlasigui, M.; Zettl, A.; Crommie, M. F. *Nat. Phys.* **2008**, *4*, 627−630.
(21) Natterer, F. D.; Zhao, Y.; Wyrick, J.; Chan, Y.-H.; Ruan, W.-Y.; Chou, M.-Y.; Watanabe, K.; Taniguchi, T.; Zhitenev, N. B.; Stroscio, J. A. *Phys. Rev. Lett.* **2015**, *114*, 245502.
(22) Jung, S.; Park, M.; Park, J.; Jeong, T.-Y.; Kim, H.-J.; Watanabe, K.; Taniguchi, T.; Han, H. D.; Hwang, C.; Kim, Y.-S. *Scientific Rep.* **2015**, *5*, 16642.
(23) Vdovin, E. E.; Mishchenko, A.; Greenaway, M. T.; Zhu, M. J.; Ghazaryan, D.; Misra, A.; Cao, Y.; Morozov, S. V.; Makarovsky, O.; Fromhold, T. M.; Patanè, A.; Slotman, G. J.; Katsnelson, M. I.; Geim, A. K.; Novoselov, K. S.; Eaves, L. *Phys. Rev. Lett.* **2016**, *116*, 186603.
(24) Yan, J.-A.; Ruan, W. Y.; Chou, M. Y. *Phys. Rev. B* **2008**, *77*, 125401.
(25) Serrano, J.; Bosak, A.; Arenal, R.; Krisch, M.; Watanabe, K.; Taniguchi, T.; Kanda, H.; Rubio, A.; Wirtz, L. *Phys. Rev. Lett.* **2007**, *98*, 095503.
(26) Mohr, M.; Maultzsch, J.; Dobardžić, E.; Reich, S.; Milošević, I.; Damnjanović, M.; Bosak, A.; Krisch, M.; Thomsen, C. *Phys. Rev. B* **2007**, *76*, 035439.
(27) Wong, D.; Velasco, J., Jr; Ju, L.; Lee, J.; Kahn, S.; Tsai, H.-Z.; Germany, C.; Taniguchi, T.; Waranabe, K.; Zettl, A.; Wanf, F.; Crommie, M. F. *Nat. Nanotechnol.* **2015**, *10*, 949−953.
(28) Xia, J.; Chen, F.; Li, J.; Tao, N. *Nat. Nanotechnol.* **2009**, *4*, 505−509.
(29) Luryi, S. *Appl. Phys. Lett.* **1988**, *52*, 501−503.
(30) Gores, J.; Goldhaber-Gordon, D.; Heemeyer, S.; Kastner, M. A.; Shtrikman, H.; Mahalu, D.; Meirav, U. *Phys. Rev. B* **2010**, *62*, 2188−2194.
(31) Liang, W.; Bockrath, M.; Bozovic, D.; Hafner, J. H.; Tinkham, M.; Park, H. *Nature* **2001**, *411*, 665−669.



DOI: 10.1021/acs.nanolett.6b04369
*Nano Lett.* 2016, 16, 7982−7987